



# Volume exclusion effects in perovskite charge transport modeling

Dilara Abdel<sup>1</sup> · Nicola E. Courtier<sup>2</sup> · Patricio Farrell<sup>1</sup>

Received: 10 March 2023 / Accepted: 27 June 2023 / Published online: 23 July 2023  
© The Author(s) 2023

## Abstract

Due to their flexible material properties, perovskite materials are a promising candidate for many semiconductor devices such as lasers, memristors, LEDs and solar cells. For example, perovskite-based solar cells have recently become one of the fastest growing photovoltaic technologies. Unfortunately, perovskite devices are far from commercialization due to challenges such as fast degradation. Mathematical models can be used as tools to explain the behavior of such devices, for example drift-diffusion equations portray the ionic and electric motion in perovskites. In this work, we take volume exclusion effects on ion migration within a perovskite crystal lattice into account. This results in the formulation of two different ionic current densities for such a drift-diffusion model – treating either the mobility or the diffusivity as density-dependent while the other quantity remains constant. The influence of incorporating each current density description into a model for a typical perovskite solar cell configuration is investigated numerically, through simulations performed using two different open source tools.

**Keywords** Perovskite modeling · Drift-diffusion equations · Volume exclusion effects · Current density

**Mathematics Subject Classification** 35Q81 · 35K57

---

✉ Dilara Abdel  
dilara.abdel@wias-berlin.de

Nicola E. Courtier  
nicola.courtier@eng.ox.ac.uk

Patricio Farrell  
patricio.farrell@wias-berlin.de

<sup>1</sup> Weierstrass Institute for Applied Analysis and Stochastics (WIAS), Mohrenstr. 39, 10117 Berlin, Germany

<sup>2</sup> Department of Engineering Science, University of Oxford, Parks Road, Oxford OX1 3PJ, UK

## 1 Introduction

Arguably, only few materials have gained such interest within photovoltaics as perovskites (Tessler and Vaynzof 2020). These materials show promise for use in applications including lasers, memristors, LEDs and solar cells. Recently, perovskite-silicon tandem cells have become more efficient than high performing single junction silicon solar cells (National Renewable Energy Laboratory (NREL) 2022). However, for the commercialization of perovskite based solar cells a couple of challenges need to be overcome, especially the fast degradation of such devices. Further, there does not exist profound knowledge about the exact physical operation mechanisms within such devices. Thus, adequate models and simulation tools are needed to better understand the device physics.

Perovskites form a class of crystalline solids of the form  $ABX_3$  with two cations A, B and an anion X which are not fixed to the crystalline lattice. To be more precise, crystal defects occur that dynamically appear and reappear. They leave void spaces, called vacancies, within the crystal which can be occupied by the migrating ions, visualized in the right unit cell in Fig. 1. This continually changing crystalline structure affects the electric charge carriers and cannot be neglected. In perovskites, the movement of numerous negatively charged anions has a strong influence on the transport of charge. A number of experimental observations and simulations indicate that ionic accumulation occurs near the perovskite interface, such as those reported by Calado et al. (2016) and Smith et al. (2018). The inclusion of ion migration can be investigated using different model approaches, for example by atomistic Density Functional Theory (DFT) calculations (e.g. Eames et al. 2015; Tan et al. 2020), equivalent circuit models (e.g. Smith et al. 2018; Moia et al. 2019) or charge transport modeling with drift-diffusion equations resulting in a system of partial differential equations. The latter approach is the most convenient one concerning the computational cost while still maintaining a direct connection of the output to the device physics. Initial charge transport models incorporating ionic movement for perovskite solar cells (PSCs) such as Calado et al. (2016), Courtier et al. (2018) or Neukom et al. (2019) were formulated, but do not limit the density of ion vacancies, meaning the presented models did not bound the number of available lattice sites within a perovskite crystal. Not limiting the ions can lead to unphysical behavior such as all ion sites becoming vacant. Especially in the context of out-of-equilibrium calculations, a model clearly needs to indicate a limit for saturation to reflect experimental observations of ionic accumulation near the interface. Later, models were introduced tackling this issue advocating for a nonlinear diffusion current density for ionic charge carriers (Abdel et al. 2021b; Calado et al. 2022) or for linear diffusion but a modified drift current density (Courtier 2019). To the best of our knowledge, the two approaches were not compared yet and their influence on a perovskite charge transport model was not assessed. The remainder of this paper is organized as follows: in Sect. 2 the

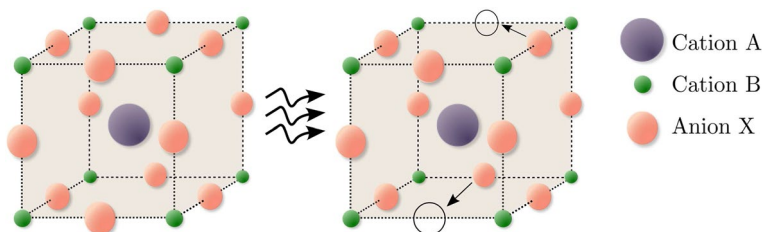


**Fig. 1** A perovskite unit cell under idealized conditions (left) and with realistic crystal defects (right). (Color figure online)

model describing charge transport in perovskites will be introduced and discussed. Afterwards, in Sect. 3 volume exclusion effects and their thermodynamically consistent inclusion into the model will be presented. This results in two different formulations of the ionic current density: treating either the mobility or the diffusivity as density-dependent while the other quantity remains constant. Then, in Sect. 4 the influence of both current density descriptions on a PSC configuration will be numerically discussed. Finally, we conclude in Sect. 5.

## 2 Model equations

Let  $\bar{\Omega} \subset \mathbb{R}^d$ ,  $d \in \{1, 2, 3\}$ , correspond to the domain of a perovskite material, which usually forms a subdomain of a full device architecture and let  $\alpha$  denote a moving charge carrier (electrons  $n$ , holes  $p$  or anion vacancies  $a$ ). Further, we define the corresponding density as  $n_\alpha$  and  $\psi$  as the electric potential. Then, the carriers' movement can be described by (Courtier et al. 2019; Abdel et al. 2021b)

$$-\nabla \cdot (\epsilon_s \nabla \psi(\mathbf{x}, t)) = \sum_{\alpha \in \{n,p,a\}} z_\alpha q (n_\alpha(\mathbf{x}, t) - C_\alpha(\mathbf{x})), \quad \mathbf{x} \in \Omega, \quad t \geq 0, \tag{1a}$$

$$z_\alpha q \partial_t n_\alpha(\mathbf{x}, t) + \nabla \cdot \mathbf{j}_\alpha(\mathbf{x}, t) = z_\alpha q r_\alpha(\mathbf{x}, t), \quad \mathbf{x} \in \Omega, \quad t \geq 0. \tag{1b}$$

Here,  $\epsilon_s$  denotes the dielectric permittivity given as the product of the relative material permittivity and the vacuum dielectric constant,  $q$  denotes the elementary charge and  $z_\alpha$  the charge number which is for electrons and holes  $z_n = -1, z_p = 1$  and for anion vacancies  $z_a = 1$ . Further, the donor and acceptor doping is given by  $C_n, C_p$  whereas the mean vacancy concentration is given by  $C_a$ . A reaction/generation mechanism can be described by a rate  $r_\alpha$ . For example, the sum total of bulk recombination mechanisms  $R$  and an external photo-generation  $G$  can be applied to both electrons and holes, i.e.  $r_n = r_p = G(\mathbf{x}) - R(n_n(\mathbf{x}, t), n_p(\mathbf{x}, t))$ . For the anion vacancies, we may assume  $r_a = 0$ . Finally, the motion of charge carriers is described by the current density  $\mathbf{j}_\alpha$ . Note that the set of unknowns can be given either in terms of the electric potential  $\psi$  and the densities of moving carriers  $n_\alpha$ ,  $\alpha = n, p, a$ , or in terms of  $(\psi, \varphi_n, \varphi_p, \varphi_a)$ , where  $\varphi_\alpha$  denotes the respective quasi Fermi potentials. These potentials are linked to the charge carrier densities via the state equation

$$n_\alpha = N_\alpha \mathcal{F}_\alpha \left( n_\alpha(\psi, \varphi_\alpha) \right), \quad n_\alpha = z_\alpha \frac{q(\varphi_\alpha - \psi) + E_\alpha}{k_B T}, \quad \alpha = n, p, a, \tag{2}$$

where  $N_n, N_p$  are the effective conduction and valence band density of states and  $E_n, E_p$  the conduction and valence band-edge energies. Further,  $N_a$  is the maximum ion vacancy concentration and  $E_a$  the formation energy. The parameter  $k_B$  refers to the Boltzmann constant and  $T$  to the temperature. We call the function  $\mathcal{F}_\alpha$ , which relates the carrier densities to the respective quasi Fermi potentials, the statistics function. For non-degenerate semiconductors the statistics function for electric charge carriers is an exponential, but in general, in the degenerate case, it is given by an integral equation, corresponding to the Fermi-Dirac integral of order 1/2 (inorganic semiconductor) or the Gauss-Fermi integral (organic semiconductor). For electrons and holes, the perovskite model (1) is supplemented with the following current density descriptions

$$\mathbf{j}_n = -qz_n(D_n \nabla n_n + z_n \mu_n n_n \nabla \psi), \quad \mathbf{j}_p = -qz_p(D_p \nabla n_p + z_p \mu_p n_p \nabla \psi), \quad (3)$$

where the diffusion coefficients  $D_n, D_p$  and the mobilities  $\mu_n, \mu_p$ , are related via the generalized Einstein relation (Abdel et al. 2021b)

$$D_\alpha = \mu_\alpha U_T g_\alpha \left( \frac{n_\alpha}{N_\alpha} \right), \quad g_\alpha \left( \frac{n_\alpha}{N_\alpha} \right) = \frac{n_\alpha}{N_\alpha} (\mathcal{F}_\alpha^{-1})' \left( \frac{n_\alpha}{N_\alpha} \right), \quad \alpha = n, p, \quad (4)$$

where  $U_T$  is the thermal voltage and  $g_\alpha$  the diffusion enhancement. When modeling non-degenerate semiconductors we have  $g_n = g_p = 1$  with constant mobilities and diffusion coefficients, but in general it holds that  $g_n, g_p \geq 1$ . Finally, to discuss physically meaningful current density descriptions for anion vacancies, volume exclusion effects need to be discussed. Note that, the model is supplemented with homogeneous (no-flux) Neumann boundary conditions for the anion vacancies as well as suitable initial and boundary conditions for all species.

### 3 Volume exclusion effects: two ionic current densities

In the fields of electrolytes and battery modeling (e.g. Borukhov et al. 2000; Bazant 2013; Sulzer et al. 2019; Landstorfer et al. 2022) or cell and molecular biology (e.g. Painter and Hillen 2002; Burger et al. 2010), the need to limit ionic (defect) concentrations is already well known. Depending on the literature this phenomenon is either called *volume exclusion effects*, *excluded-volume effects*, *steric effects*, *volume filling* or *limitation of overcrowding*. Within our framework this means that the finite number of available lattice sites within a crystalline semiconductor needs to be incorporated into the charge transport model. Within our framework, this can be done by limiting the vacancy accumulation via a saturation limit  $N_a$ , which is physically bounded by

$$C_a \leq N_a \leq \bar{N}_a := 3n_L.$$

Here,  $C_a$  denotes the average anion vacancy density entering the Poisson equation (1a) on the right-hand side and the upper bound  $\bar{N}_a$  is defined as the lattice density  $n_L$  multiplied with the number of halogen sites in a unit cell. The saturation limit  $N_a$  is a model parameter, but  $C_a$  and  $\bar{N}_a$  remain fixed for a given perovskite. The average vacancy concentration for MAPI ranges from approximately  $C_a = 1.0 \times 10^{17}$  to  $1.6 \times 10^{19} \text{cm}^{-3}$  (see Walsh et al. (2015), Richardson et al. (2016)), while the upper bound equals  $\bar{N}_a = 1.21 \times 10^{22} \text{cm}^{-3}$  for a lattice constant of  $6.28 \text{ \AA} = 6.28 \times 10^{-8} \text{cm}$  according to Eames et al. (2015).

Figure 2 visualizes the vacancy density  $n_a$  for different choices of the saturation limit  $N_a$ , including the two special cases of suppressing vacancy movement (left) or choosing the saturation limit equal to the largest bound  $\bar{N}_a$  (right). Experimentally observed accumulation of vacancies may be reproduced for a saturation limit  $N_a$  between these two saturation limit bounds. Hence, we can identify  $N_a$  as a model parameter limiting the vacancy accumulation. To include volume exclusion effects in a thermodynamically consistent manner, we use a statistical relation as in (2) for the anion vacancies given by the Fermi-Dirac integral of order  $-1$ , which is bounded by zero and one,

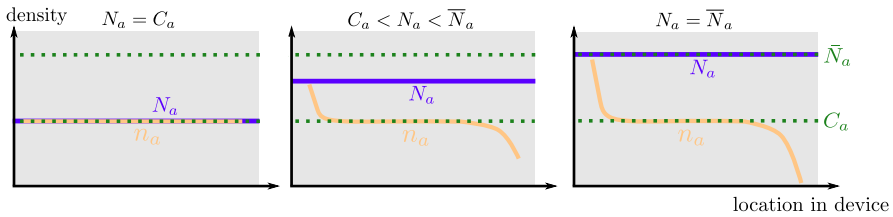


**Fig. 2** Three possible vacancy density configurations depending on the choice of the saturation limit  $N_a$ . The left and right panels visualize the case, where  $N_a$  equals its lower or upper bound, respectively. The value of the maximum vacancy density  $N_a$  can be chosen to ensure that, e.g., experimentally observed accumulation is correctly limited (middle panel). (Color figure online)

$$n_a = N_a \mathcal{F}_a \left( \eta_a(\psi, \varphi_a) \right) = \frac{N_a}{\exp(-\eta_a) + 1}, \quad \eta_a = \frac{q(\varphi_a - \psi) + E_a}{k_B T}. \tag{5}$$

Note that  $z_a q \varphi_a$  is frequently called the electrochemical potential, but to be consistent with semiconductor theory, we refer to it as a quasi Fermi potential. Now, possible descriptions for the ion vacancy current density  $\mathbf{j}_a$  can be discussed. We start from this formulation

$$\mathbf{j}_a = -q \mu_a z_a^2 n_a \nabla \varphi_a,$$

showing the proportionality of the charge carrier current density to its thermodynamic driving force—the negative gradient of the quasi Fermi potential. For diffusion on a lattice, the generalized Einstein relation between the diffusion coefficient and mobility of the anion vacancies likewise holds (Bazant 2013)

$$D_a = \mu_a U_T g_a \left( \frac{n_a}{N_a} \right), \quad g_a \left( \frac{n_a}{N_a} \right) = \frac{1}{1 - \frac{n_a}{N_a}}, \tag{6}$$

where  $g_a$  is sometimes called the activity coefficient instead of diffusion enhancement. Whether we assume now a constant mobility or a constant diffusivity results in two different drift-diffusion current density descriptions.

*Nonlinear diffusion* On the one hand, to be consistent with the electron and hole flux descriptions we can assume a constant mobility  $\mu_a = \bar{\mu}_a$ , apply the generalized Einstein relation (6) and make use of the state equation (5) such that the current density comprises nonlinear diffusion (Abdel et al. 2021b)

$$\mathbf{j}_{a,\text{diff}} = -q z_a \bar{\mu}_a U_T \left( g_a \left( \frac{n_a}{N_a} \right) \nabla n_a + \frac{z_a}{U_T} n_a \nabla \psi \right). \tag{7}$$

*Modified drift* On the other hand, a constant diffusion coefficient  $D_a = \bar{D}_a$ , called the chemical diffusivity, allows us to express the mobility in terms of the activity coefficient  $g_a$ . This leads to a current density expression with linear diffusion but with a modified drift term (Bazant 2013; Courtier 2019)

$$\mathbf{j}_{a,\text{drift}} = -q z_a \bar{D}_a \left( \nabla n_a + \frac{z_a}{U_T g_a \left( \frac{n_a}{N_a} \right)} n_a \nabla \psi \right). \tag{8}$$

Assuming that the constant prefactors in both current density descriptions are proportional, i.e.  $\bar{\mu}_a U_T \sim \bar{D}_a$ , leads to

$$\mathbf{j}_{a,\text{diff}} \sim g_a \left( \frac{n_a}{N_a} \right) \mathbf{j}_{a,\text{drift}}. \quad (9)$$

Hence, if  $\bar{\mu}_a U_T \sim \bar{D}_a$ , then the main difference between the nonlinear diffusion and the modified drift current density is the additional diffusion enhancement as prefactor. Note that both current densities, (7) and (8), lead to two *different* charge transport models which have the *same* steady state solution due to the homogeneous Neumann boundary condition. To the best of our knowledge, there does not exist a work where the influence of both current density descriptions on the charge transport model behavior for perovskites was compared and investigated. Thus, in the following we look closer at the numerical performances of the two current densities introduced in (7) and (8).

#### 4 Numerical simulation of a PSC device

In this section, we simulate a three-layer PSC device, where the perovskite is sandwiched between two doped non-perovskite semiconductor transport layers. To be more precise, MAPI is used as the perovskite material, while PCBM is chosen for the electron and PEDOT:PSS for the hole transport layer. A schematic of the device architecture is shown in Fig. 3. Note that anion vacancies move solely within the perovskite (red area), whereas electrons, holes and the electric potential are defined across the whole device.

*Designing the benchmark* Let us introduce the dimensionless scaling factor

$$\epsilon = \frac{C_a}{N_a} = \frac{\text{average anion vacancy density}}{\text{maximum anion vacancy density}},$$

where the fixed value of  $C_a$  is incorporated into the model via the right-hand side of the Poisson equation (1a) and  $N_a$  is a model parameter in the state equation (5). If  $\epsilon$  tends to zero, then we neglect the finite size of ions, resulting in a Boltzmann relation between  $n_a$  and  $\varphi_a$  (meaning  $\mathcal{F}_a \approx \exp$ ). Contrarily, if  $\epsilon = 1$ , then ionic movement is suppressed and, thus, the model reduces to the classical van Roosbroeck system. Therefore, a small  $\epsilon$  indicates *low exclusion*, while a larger  $\epsilon$  indicates *high exclusion*. A lower limit of 0.004 for  $\epsilon$  may be calculated by taking an estimate for the maximum possible vacancy density and an estimate for  $C_a$  from DFT calculations as performed by Walsh et al. (2015). However, the precise choice of  $\epsilon$  is strongly dependent on the perovskite material. In the definition of  $\epsilon$ , we keep the average density of vacancies  $C_a$  the same. Instead, we discuss maximum vacancy densities  $N_a$  that are lower than those previously assumed, i.e., we choose  $N_a < \bar{N}_a$ . Indeed, in the context of solid oxide cells with YSZ as electrolyte material, Miloš

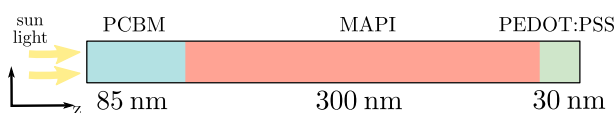


**Fig. 3** Schematic diagram of the simulated device configuration with ohmic contacts. The electron transport layer (blue) is given by PCBM, whereas for the hole transport layer (green) PEDOT:PSS is used. (Color figure online)

et al. (2022) formulated a similar model for mobile ionic carriers, where a saturation limit  $N_a$  smaller than  $\bar{N}_a$  was successfully fitted to measurements. For clarity, one can consider variations in  $\epsilon$  to represent different maximum vacancy densities, since only a certain percentage of ion sites, rather than all, becoming vacant is sufficient to observe accumulation. Hence,  $\epsilon$  measures the degree of vacancy accumulation. Given sufficient relaxation time, a charge transport model of the form (1) on a domain as depicted in Fig. 3 based on either (7) or (8) results in the same steady state solution. Thus, of special interest is the simulation of current–voltage (J–V) scan protocols, where the model is far from an equilibrium state. For this, we simulate a linear J–V scan protocol with a scan rate of 40mV/s for an applied bias between 0V and 1.2V. This implies that the scan ends at  $t = 30$  s. Note, that during the scan the outer boundary conditions for the ohmic contacts vary with time and the steady state is not reached. The simulations were performed in one dimension and the chosen parameters can be found in Table 1. We choose  $\bar{\mu}_a = 1 \times 10^{-10} \text{cm}^2/(\text{Vs})$  and  $\bar{D}_a = 2.59 \times 10^{-12} \text{cm}^2/\text{s}$ . By construction, we have  $\bar{\mu}_a U_T = \bar{D}_a$ .

To simulate the PSC device, we make use of two open source tools `Ionmonger` (Courtier et al. 2018, 2019) and `ChargeTransport.jl` (Abdel et al. 2021a, 2022). While `ChargeTransport.jl` uses a finite volume method for the spatial discretization implemented in Julia, `Ionmonger` is based on a finite element method written in Matlab. The same non-uniform grid spacing as introduced by Courtier et al. (2019) is used, whereas a uniform time mesh is utilized in `ChargeTransport.jl` and an adaptive one in `IonMonger`. To primarily focus on the impact of the different current density descriptions, other effects such as photo-generation and surface recombination are neglected in the simulations.

*Electric potential and vacancy density profiles* Fig. 4 shows the evolution of the electric potential within the perovskite layer (area shaded in red). Additionally, the evolution of the vacancy density in the vicinity of each perovskite/transport layer interface is depicted

**Table 1** Parameter values at a temperature  $T = 300\text{K}$  (Calado et al. 2022)

Physical quantity	Symbol	Value			Unit
		PCBM	Perovskite	PEDOT:PSS	
Layer thickness		$8.5 \times 10^{-6}$	$3.0 \times 10^{-5}$	$3.0 \times 10^{-6}$	cm
Relative permittivity		3	23	4	
Conduction band-edge energy	$E_n$	-3.8	-3.8	-3.0	eV
Valence band-edge energy	$E_p$	-6.2	-5.4	-5.1	eV
Eff. conduction bandDoS	$N_n$	$1 \times 10^{19}$	$1 \times 10^{19}$	$1 \times 10^{20}$	$\text{cm}^{-3}$
Eff. valence band DoS	$N_p$	$1 \times 10^{19}$	$1 \times 10^{19}$	$1 \times 10^{20}$	$\text{cm}^{-3}$
Mean anion vacancy density	$C_a$	–	$1.0 \times 10^{18}$	–	$\text{cm}^{-3}$
Doping density	$C_n$	$2.09 \times 10^{18}$	0.0	0.0	$\text{cm}^{-3}$
Doping density	$C_p$	0.0	0.0	$2.09 \times 10^{18}$	$\text{cm}^{-3}$
Electron mobility	$\mu_n$	$1 \times 10^{-3}$	20	0.1	$\text{cm}^2/(\text{Vs})$
Hole mobility	$\mu_p$	$1 \times 10^{-3}$	20	0.1	$\text{cm}^2/(\text{Vs})$
Radiative recombination coeff		0.0	$3.6 \times 10^{-12}$	0.0	$\text{cm}^3/\text{s}$
SRH lifetimes (electrons & holes)		$1.0 \times 10^{100}$	$1.0 \times 10^{-7}$	$1.0 \times 10^{100}$	s
SRH trap energy		-5.0	-4.6	-4.05	eV

SRH denotes Shockley–Read–Hall recombination

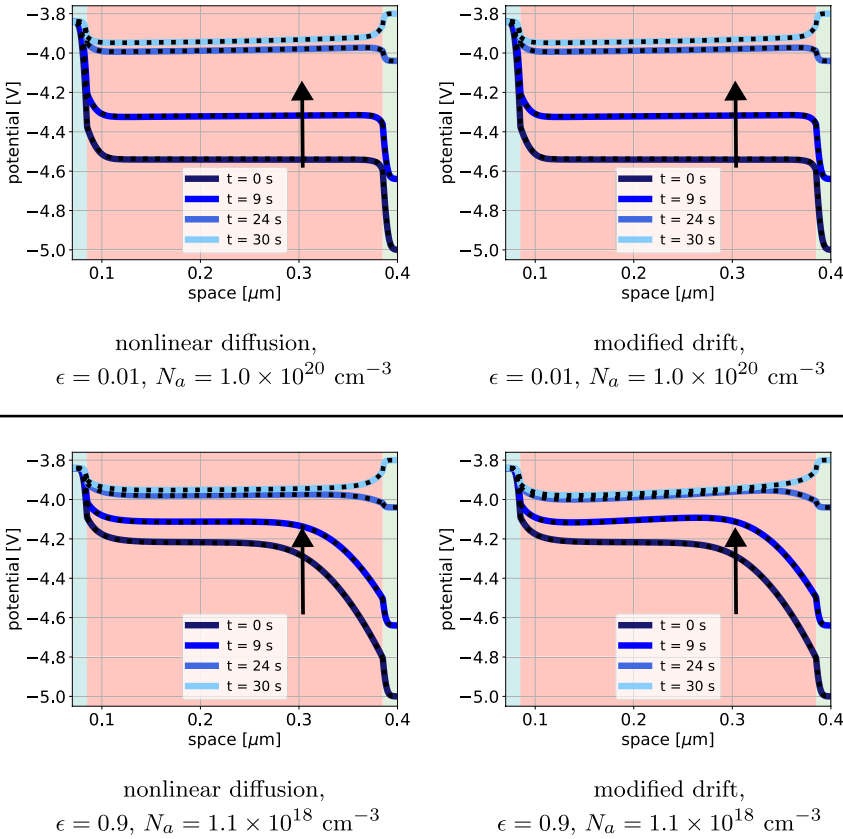


**Fig. 4** Evolution of the electric potential  $\psi$  in the perovskite layer solving the model (1) based on the nonlinear diffusion current density (7) (first column) and for the model based on the modified drift current (8) (second column). The first row shows the case of  $\epsilon = 0.01$  (low exclusion,  $E_a = -4.66$  eV) and the second row of  $\epsilon = 0.9$  (high exclusion,  $E_a = -4.16$  eV). The arrows indicate the direction of increasing time. (Color figure online)

in Fig. 5. Both profiles are visualized for a model based on the nonlinear diffusion current density (7) and a model based on the modified drift current (8) for two choices of  $\epsilon$  reflecting low and high volume exclusion. The colored lines correspond to a solution calculated with `ChargeTransport.jl` whereas the black dotted lines indicate respective solutions calculated with `Ionmonger`. Brighter colors indicate later time. First, note that both software tools based on different discretization techniques yield near-identical results. Hence, we can compare the impact of the different current density descriptions independent of the numerical method. Not surprisingly, for  $\epsilon = 0.01$  no difference in the electrostatic potential evolution (Fig. 4, first row) and in the vacancy density profiles (Fig. 5, top set of four) can be observed. Contrarily for high volume exclusion, i.e. larger  $\epsilon$ , the modified drift current density (8) causes a slower decrease of the ion density at the right perovskite interface (Fig. 5, second set of rows). In the case of high exclusion, the flux of ions is limited by restricting on the number of free lattice sites. In the case of nonlinear diffusion, this restriction is counterbalanced by the diffusion enhancement factor, which increases the diffusivity of the ions and hence the timescale of motion. The slower diffusivity can be seen



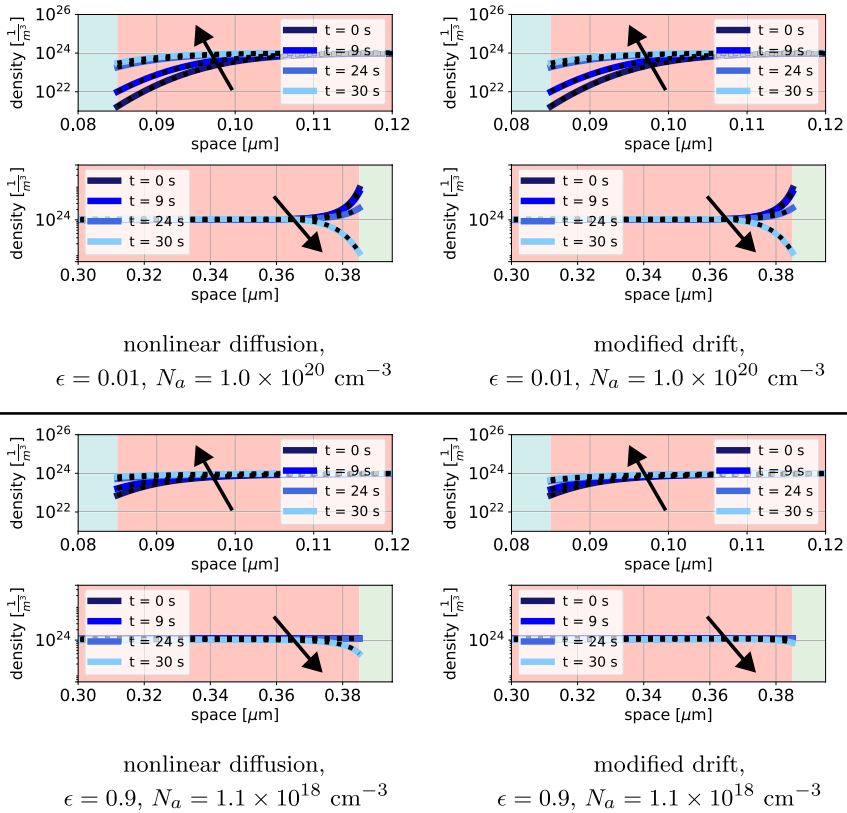


**Fig. 5** Evolution of the vacancy density  $n_a$  at the left and right perovskite/transport layer interface for the model based on the nonlinear diffusion current (7) (first column) and for a model based on the modified drift current (8) (second column). The first set of rows shows the case of  $\epsilon = 0.01$  ( $E_a = -4.66$  eV) and the second set of rows (below the line) corresponds to  $\epsilon = 0.9$  ( $E_a = -4.16$  eV). The arrows indicate the direction of increasing time. No differences can be observed in the case of low exclusion, whereas a slower evolution of the ion profile can be observed in the case of high exclusion and a modified drift current density. (Color figure online)

in the equations by relation (9) and the choice of  $\bar{\mu}_a U_T = \bar{D}_a$  in our simulation. Therefore, it is only in the case of both high exclusion and modified drift (Fig. 5, second set of rows) that we see a slower evolution. Additionally, the electric potential gradients remain larger for the modified drift approach for larger times such as  $t = 24$  s and  $t = 30$  s in Fig. 4 (second row). Furthermore, Fig. 6 shows that the difference in the calculated electric potentials, i.e.  $\psi_{\text{drift}} - \psi_{\text{diff}}$ , is approximately two orders of magnitude larger for high volume exclusion. Even though the difference in the electric potentials (Fig. 6) behaves similarly for all depicted times  $t$ , Fig. 7 indicates in the case of high excluded-volume effects the difference in the vacancy density at the end time  $t = 30$  s is comparably large. This trend can be likewise observed for different choices of  $\epsilon$  in Fig. 8, where the  $L^\infty$  error between the calculated electric potentials and the vacancy densities with respect to  $\epsilon$  are depicted. Both  $L^\infty$  errors are increasing with higher effects of excluded-volume for all visualized times  $t > 0$ . It seems that the difference in the vacancy densities becomes most visible for larger times and larger  $\epsilon$  (Fig. 8, right) and increases the most for the end time  $t = 30$  s.

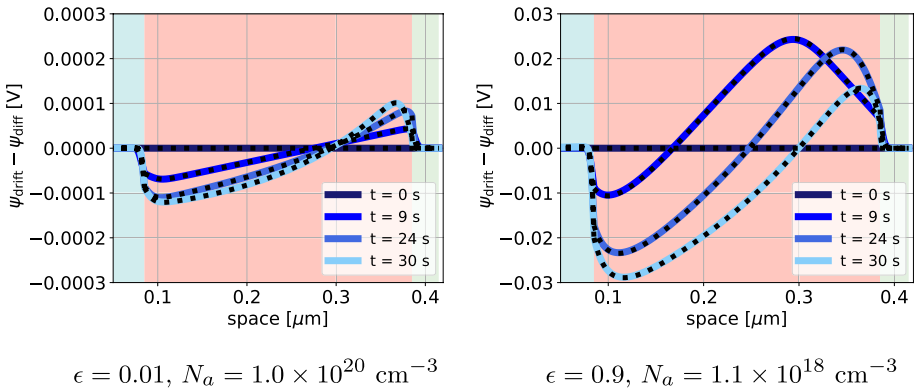


**Fig. 6** Difference between calculated electrostatic potentials depicted in Fig. 4 based on either a modified drift or a nonlinear diffusion approach, i.e. the error  $\psi_{\text{drift}} - \psi_{\text{diff}}$  is shown for  $\epsilon = 0.01$  (left) and  $\epsilon = 0.9$  (right). The scale of the y-axes differs by two orders of magnitudes. (Color figure online)

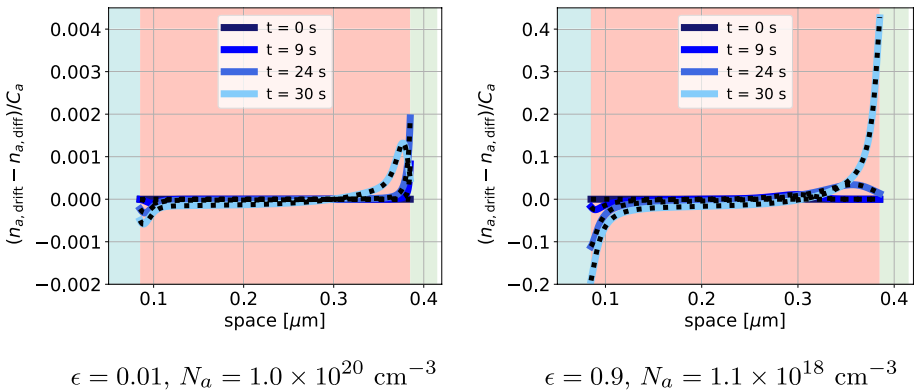


**Fig. 7** Difference between calculated vacancy densities depicted in Fig. 5 based on either a modified drift or a nonlinear diffusion approach scaled by the average vacancy density for  $\epsilon = 0.01$  (left) and  $\epsilon = 0.9$  (right). The scale of the y-axes differs by two orders of magnitudes. (Color figure online)

Note that the end time here does not refer to a steady state, but to the end time of the scan protocol. Thus, we can conclude that in the case of high volume exclusion the time scales of converging towards a steady state for a model based on either nonlinear diffusion or on a modified drift current density are diverging.

*Current–voltage curves* Lastly, the influence of the different current density descriptions on J-V curves (simulated in the dark) is investigated in Figs. 9 and 10. Again, colored curves correspond to solutions calculated with `ChargeTransport.jl`, while black dotted lines are the solutions received when using `IonMonger`. Brighter colors indicate higher volume exclusion which is reflected in the choice of  $\epsilon$ . First, both approaches reveal in Fig. 9 that the larger the choice for  $\epsilon$ , the more the respective J-V curve is shifted to the left, i.e. the higher the recombination rate. Second, when employing the modified drift approach a greater change in the J-V curves with respect to the difference between the smallest and largest  $\epsilon$  can be noticed (see Fig. 9). Third, for the model based on the modified drift current density, the impact of volume exclusion becomes observable in the J-V

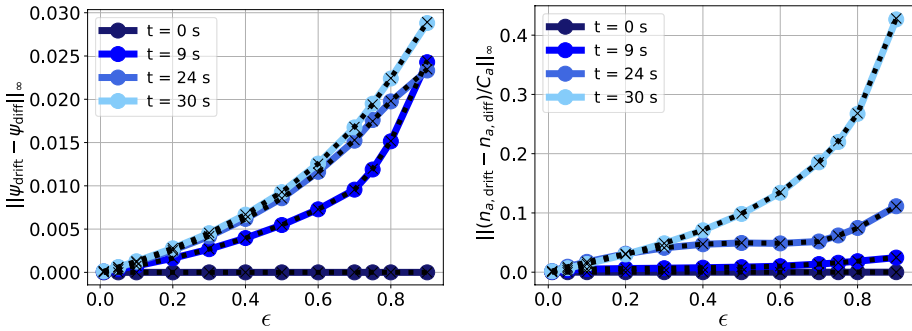


**Fig. 8**  $L^\infty$  error between the electric potentials (left) and the vacancy densities (right) calculated from a model based on either a nonlinear diffusion or a modified drift current density for different values of  $\epsilon$ . (Color figure online)

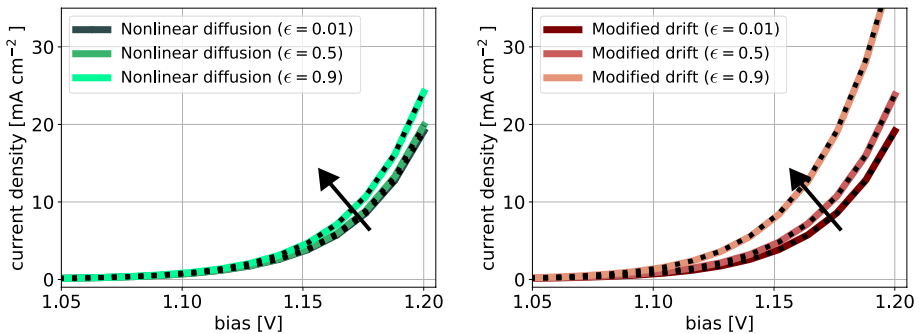


**Fig. 9** Current–voltage curves for nonlinear diffusion (left) and modified drift (right) for variations of  $\epsilon$ . The arrows indicate the direction of increasing  $\epsilon$ . For larger values of  $\epsilon$  the diode opens earlier. (Color figure online)

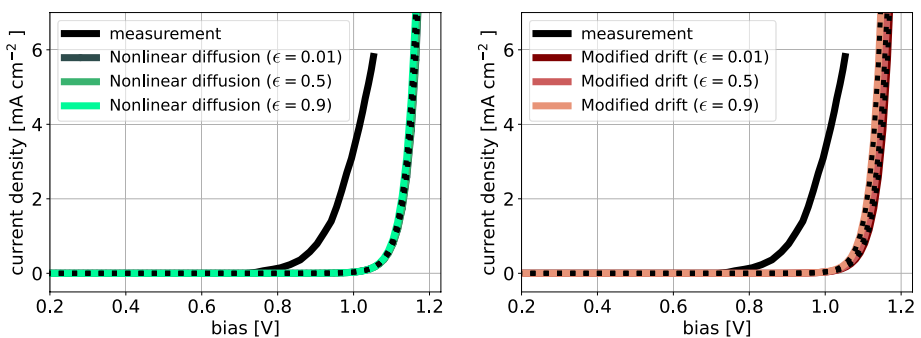


**Fig. 10** Simulated current–voltage curves for nonlinear diffusion (left) and modified drift (right) for variations of  $\epsilon$  in comparison with measurement curves from Calado et al. (2016). (Color figure online)

curves at a smaller value of  $\epsilon$ . The trends in the recombination current can be explained, as in Courtier (2020), in terms of the distribution of the electric potential across the cell. In this model, the dominant form of recombination is hole-limited bulk SRH recombination.

At earlier times ( $t = 0$  s and  $t = 9$  s in Fig. 4), it can be seen that low exclusion leads to smaller potential drops within the perovskite layer and larger potential drops within the neighboring transport layers. Large drops can suppress recombination (by keeping minority carriers away from recombination sites) by forming barriers. However, at later times ( $t = 24$  s and  $t = 30$  s), we observe that the electric field at the perovskite/HTL interface decreases for increasing  $\epsilon$ . Smaller positive fields/larger negative fields allow a greater number of holes from the transport layer to enter the perovskite, leading to increased recombination and higher currents, as shown in Fig. 9. For the modified drift current density, at large  $\epsilon$ , a negative electric field also emerges across the bulk of the perovskite due to the slower migration of ions (see Fig. 5, second set of rows), which further enhances the rate of recombination. Note that surface recombination was neglected in our simulations, since, in comparison to the large density of ionic defects in MAPI, electronic charge carriers have a negligible effect on the distribution of the electric field, particularly at steady state. A non-constant, but small surface recombination in our simulations would not significantly change our results for the ion or potential profiles, but would lead to an increased total recombination and higher currents. In Fig. 10, the simulated J–V curves are compared to the measured curves from Calado et al. (2016) for the same device set-up as illustrated in Fig. 3. Now, one may argue that the difference between either nonlinear diffusion or modified drift current density may be minor. But, for the sake of simplicity, other effects such as surface mechanisms were entirely neglected in this study. Additional physical effects may exhibit different behavior depending on whether a charge transport model is based on nonlinear diffusion or modified drift current densities. Thus, it is important to develop the capabilities to investigate the underlying ion migration mechanism in order to formulate accurate device models.

## 5 Summary and Outlook

For a perovskite charge transport model we discussed how to properly include volume exclusion effects via the statistics function in the case of migrating ionic charge carriers. This study provides two possible current density descriptions: nonlinear diffusion (7) and a modified drift (8). Both descriptions recover special cases of the charge transport model in the limit of ignoring the finite size of ions or suppressing ionic movement. Further, the models based on both current density descriptions converge towards the same steady solution. In numerical simulations, the influence of both descriptions on the internal states and on the current–voltage behavior of a three-layer PSC configuration was investigated. The simulations were performed with two different open source tools based on different numerical methods of solution, yielding near-identical results. In the case of high exclusion, the modified drift current leads to a slower evolution of the ion profile. This reveals a greater influence of volume exclusion effects on model predictions based on a modified drift current density description. Studying the impact of these approaches for a generalized charge transport model including further physically meaningful mechanisms is of interest in the future. Also, studying the impact on the performance of alternative device architectures based on other perovskite and transport layer materials can be a topic of future research. Finally, the parameter sensitivity of other physical quantities such as band-edge energies or the dielectric permittivity was neglected even though they have an impact on the electric potential and thus on the vacancy density behavior. This could also be investigated in a continuation of this work.

**Author Contributions** All authors read, edited and approved the manuscript. DA: Material preparation, Data collection, Investigation, Software, Writing - original draft. NEC: Software, Writing—review & editing, Supervision. PF: Software, Writing—review & editing, Supervision.

**Funding** Open Access funding enabled and organized by Projekt DEAL. This work was partially supported by the Leibniz competition 2020 (NUMSEMIC, J89/2019).

**Availability of data and materials** The datasets can be generated with the presented open software tools `ChargeTransport.jl` (<https://github.com/PatricioFarrell/ChargeTransport.jl>) and `Ionmonger` (<https://github.com/PerovskiteSCModelling/IonMonger>) available on GitHub.

## Declarations

**Conflict of interest** The authors have no relevant financial or non-financial interests to disclose.

**Ethical approval** Not applicable.

**Open Access** This article is licensed under a Creative Commons Attribution 4.0 International License, which permits use, sharing, adaptation, distribution and reproduction in any medium or format, as long as you give appropriate credit to the original author(s) and the source, provide a link to the Creative Commons licence, and indicate if changes were made. The images or other third party material in this article are included in the article's Creative Commons licence, unless indicated otherwise in a credit line to the material. If material is not included in the article's Creative Commons licence and your intended use is not permitted by statutory regulation or exceeds the permitted use, you will need to obtain permission directly from the copyright holder. To view a copy of this licence, visit <http://creativecommons.org/licenses/by/4.0/>.

## References

- Abdel, D., Farrell, P., Fuhrmann, J.: Assessing the quality of the excess chemical potential flux scheme for degenerate semiconductor device simulation. *Opt. Quantum Electron.* **53**(163), 15 (2021)
- Abdel, D., Farrell, P., Fuhrmann, J.: ChargeTransport.jl: simulating charge transport in semiconductors (2022). <https://doi.org/10.5281/zenodo.6275688>
- Abdel, D., Vágner, P., Fuhrmann, J., et al.: Modelling charge transport in perovskite solar cells: potential-based and limiting ion depletion. *Electrochim. Acta* **390**(138), 696 (2021)
- Bazant, M.Z.: Theory of chemical kinetics and charge transfer based on nonequilibrium thermodynamics. *Acc. Chem. Res.* **46**(5), 1144–1160 (2013)
- Borukhov, I., Andelman, D., Orland, H.: Adsorption of large ions from an electrolyte solution: a modified Poisson–Boltzmann equation. *Electrochim. Acta* **46**(2), 221–229 (2000)
- Burger, M., Di Francesco, M., Pietschmann, J.F., et al.: Nonlinear cross-diffusion with size exclusion. *SIAM J. Math. Anal.* **42**(6), 2842–2871 (2010)
- Calado, P., Telford, A., Bryant, D., et al.: Evidence for ion migration in hybrid perovskite solar cells with minimal hysteresis. *Nat. Commun.* **7**, 13831 (2016)
- Calado, P., Gelmetti, I., Hilton, B., et al.: Driftfusion: an open source code for simulating ordered semiconductor devices with mixed ionic-electronic conducting materials in one dimension. *J. Comput. Electron.* **21**, 1–32 (2022)
- Courtier, N.E., Richardson, G., Foster, J.M.: A fast and robust numerical scheme for solving models of charge carrier transport and ion vacancy motion in perovskite solar cells. *Appl. Math. Model.* **63**, 329–348 (2018)
- Courtier, N.E.: Modelling ion migration and charge carrier transport in planar perovskite solar cells. Ph.D Thesis, University of Southampton (2019)
- Courtier, N.E.: Interpreting ideality factors for planar perovskite solar cells: ctypal diode theory for steady-state operation. *Phys. Rev. Appl.* **14**(2), 024,031 (2020)

- Courtier, N.E., Cave, J.M., Walker, A.B., et al.: Ionmonger: a free and fast planar perovskite solar cell simulator with coupled ion vacancy and charge carrier dynamics. *J. Comput. Electron.* **18**, 1435–1449 (2019)
- Eames, C., Frost, J.M., Barnes, P.R.F., et al.: Ionic transport in hybrid lead iodide perovskite solar cells. *Nat. Commun.* **6**(1), 7497 (2015)
- Landstorfer, M., Ohlberger, M., Rave, S., et al.: A modelling framework for efficient reduced order simulations of parametrised lithium-ion battery cells. *Eur. J. Appl. Math.* **34**(3), 554–591 (2023)
- Miloš, V., Vágner, P., Budáč, D., et al.: Generalized Poisson–Nernst–Planck-based physical model of the O<sub>2</sub> LSM|YSZ electrode. *J. Electrochem. Soc.* **169**(4), 044,505 (2022). <https://doi.org/10.1149/1945-7111/ac4a51>
- Moia, D., Gelmetti, I., Calado, P., et al.: Ionic-to-electronic current amplification in hybrid perovskite solar cells: ionically gated transistor-interface circuit model explains hysteresis and impedance of mixed conducting devices. *Energy Environ. Sci.* **12**, 1296–1308 (2019)
- National Renewable Energy Laboratory (NREL): Best research-cell efficiency chart (2022). <https://www.nrel.gov/pv/cell-efficiency.html>. Accessed 30 Sept 2022
- Neukom, M.T., Schiller, A., Züfle, S., et al.: Consistent device simulation model describing perovskite solar cells in steady-state, transient, and frequency domain. *ACS Appl. Mater. Interfaces* **11**(26), 23,320–23,328 (2019)
- Painter, K., Hillen, T.: Volume-filling and quorum-sensing in models for chemosensitive movement. *Can. Appl. Math. Quart.* **10**, 501–543 (2002)
- Richardson, G., O’Kane, S.E.J., Niemann, R.G., et al.: Can slow-moving ions explain hysteresis in the current-voltage curves of perovskite solar cells? *Energy Environ. Sci.* **9**, 1476–1485 (2016). <https://doi.org/10.1039/C5EE02740C>
- Smith, E.C., Ellis, C.L.C., Javaid, H., et al.: Interplay between ion transport, applied bias, and degradation under illumination in hybrid perovskite p-i-n devices. *J. Phys. Chem. C* **122**(25), 13,986–13,994 (2018)
- Sulzer, V., Chapman, S.J., Please, C.P., et al.: Faster lead-acid battery simulations from porous-electrode theory: part I. physical model. *J. Electrochem. Soc.* **166**(12), A2363–A2371 (2019)
- Tan, S., Yavuz, I., De Marco, N., et al.: Steric impediment of ion migration contributes to improved operational stability of perovskite solar cells. *Adv. Mater.* **32**(11), 1906,995 (2020)
- Tessler, N., Vaynzof, Y.: Insights from device modeling of perovskite solar cells. *ACS Energy Lett.* **5**(4), 1260–1270 (2020)
- Walsh, A., Scanlon, D.O., Chen, S., et al.: Self-regulation mechanism for charged point defects in hybrid halide perovskites. *Angew. Chem. Int. Ed.* **54**(6), 1791–1794 (2015)

**Publisher’s Note** Springer Nature remains neutral with regard to jurisdictional claims in published maps and institutional affiliations.